

A Dual-Band Multilayer InSe Self-Powered Photodetector with High Performance Induced by Surface Plasmon Resonance and Asymmetric Schottky Junction

Mingjin Dai,^{†,‡,||} Hongyu Chen,^{*,‡,§} Rui Feng,[§] Wei Feng,[†] Yunxia Hu,^{†,‡} Huihui Yang,^{†,‡} Guangbo Liu,[‡] Xiaoshuang Chen,[‡] Jia Zhang,[‡] Cheng-Yan Xu,^{†,||} and PingAn Hu^{*,‡,||,||}

[†]School of Materials Science and Engineering, [‡]MOE Key Laboratory of Micro-Systems and Micro-Structures Manufacturing,

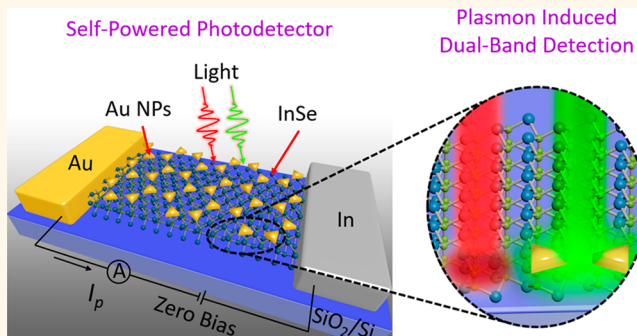
[§]Department of Physics, and ^{||}State Key Laboratory of Robotics and Systems, Harbin Institute of Technology, Harbin 150080, P. R. China

¹Department of Chemistry and Chemical Engineering, College of Science, Northeast Forestry University, Harbin 150040, P. R. China

Supporting Information

ABSTRACT: A dual-band self-powered photodetector (SPPD) with high sensitivity is realized by a facile combination of InSe Schottky diode and Au plasmonic nanoparticle (NP) arrays. Comparing with pristine InSe devices, InSe/Au photodetectors possess an additional capability of photodetection in visible to near-infrared (NIR) region. This intriguing phenomenon is attributed to the wavelength selective enhancement of pristine responsivities by hybridized quadrupole plasmons resonance of Au NPs. It is worth pointing out that the maximum of enhancement ratio in responsivity reaches up to ~1200% at a wavelength of 685 nm. In addition, owing to a large Schottky barrier difference formed between active layer and two asymmetric electrodes, the responsivities of dual-band InSe/Au photodetector could reach up to 369 and 244 mA/W at the wavelength of 365 and 685 nm under zero bias voltage, respectively. This work would provide an additional opportunity for developing multifunctional photodetectors with high performance based on two-dimensional materials, upgrading their capacity of photodetection in a complex environment.

KEYWORDS: InSe, dual-band, self-powered photodetector, quadrupole, plasmonic enhancement



Multiband photodetectors whose working spectral range from UV throughout visible to infrared (IR) have received prodigious attention due to their broad applications in imaging techniques, light-wave communications, optical guidance technology, environment monitoring, etc.^{1–3} By identifying the target on the basis of distinguishable spectrum response, multiband information obtained by this technology could upgrade capacity of photodetection in a complex environment. Furthermore, for applications in several extreme conditions, self-powered photodetectors with a smaller size which can work without an external power source are also highly desired.^{4–7} Although SPPDs have received increasing attention in the past few years, most of present photodetectors still need external bias voltage to satisfy the needs of practical application. Therefore, self-

driven multiband photodetectors with high sensitivity are still lacking.

Over the past few decades, significant developments in fabricating dual-band or multiband photodetectors have been achieved by epitaxial growth of alloy semiconductors, 2D materials heterojunction, superlattices, and multiple quantum well structure, etc.^{1,8–11} However, their active layer semiconductor materials were generally constructed by using sophisticated instruments, such as molecular beam epitaxy, metal organic chemical vapor deposition, atomic layer deposition, and so on. With the rapid developments in

Received: June 29, 2018

Accepted: August 10, 2018

Published: August 10, 2018

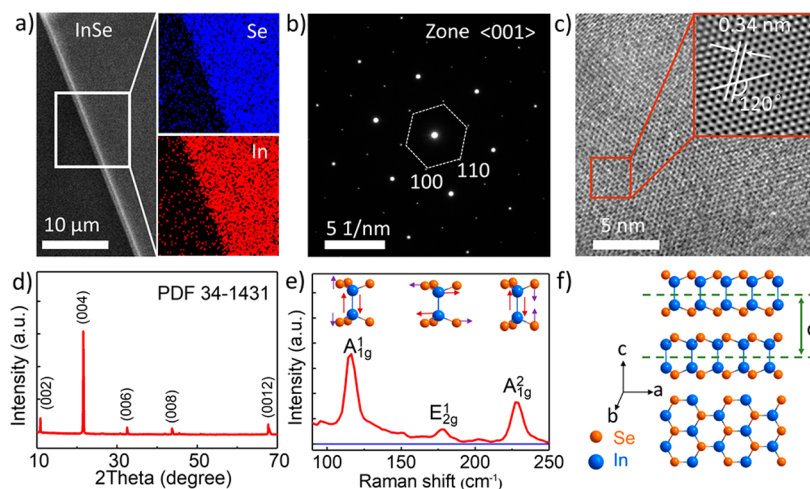


Figure 1. Crystal structure and characterization of InSe nanosheets. (a) SEM image of InSe nanosheets and EDX mapping of Se and In elements. (b) SAED pattern with an orientation along the [001] zone axis. (c) HRTEM image for InSe nanosheets. Inset: The corresponding reverse Fourier transform pattern. (d) XRD pattern of InSe nanosheets. (e) Raman spectrum (red line) of InSe nanosheets on SiO₂/Si substrate. Blue line is the baseline. (f) Side and top views of the InSe crystal structure with a monolayer thickness of $d = 0.83$ nm.

material science, some convenient methods such as mechanical exfoliation and chemical vapor deposition, etc., have been developed to fabricate ultrathin 2D semiconductor materials with low cost.^{12–16} However, it is difficult for a two-dimensional (2D) semiconductor material to build a multi-band photodetector with high detectivity by taking its natural advantages. As an excellent rising star of 2D III–VI compounds semiconductor, InSe has a smaller electron effective mass ($m^* = 0.143 m_0$) compared with MoS₂ ($m^* = 0.45 m_0$), and the electronic devices based on InSe few-layers exhibit high mobility over 10^3 cm² V⁻¹ s⁻¹ at room temperature.^{17,18} In addition, a direct band gap ($E_g = 1.26$ eV) at room temperature, which can increase up to 1.42 eV when its thickness is down to ~ 6 nm, reveals a large spread of band gaps in the NIR region.¹⁹ Nevertheless, most of present InSe-based photodetectors can only operate with a high responsivity in the short wavelength region, limiting their ability of photodetection in visible or NIR region.^{16,20}

Fortunately, with the ability to route and manipulate light at nanoscale beyond the diffraction limit, plasmonic technique offers opportunities to improve the quantum efficiency of photodetectors with high wavelength selectivity.^{21–23} This allows one to tailor the surface plasmon resonance frequency and enhance photoelectric conversion efficiency in a desirable wavelength range and provides a possible pathway to realize InSe-based dual-band or multiband photodetectors. Therefore, we proposed a dual-band InSe-based asymmetry Schottky junction photodetector in conjunction with plasmonic technique. The InSe/Au device exhibits a high responsivity of 369 mA/W at the wavelength of 365 nm with a high on–off ratio up to 10^3 without any power supply, which is much higher than that of traditional UV SPPDs. More interestingly, compared with pristine InSe photodetector which can only operate in UV-vis short-wavelength region, InSe/Au device possesses an ability of dual-band photodetection in UV–vis–NIR broadband region. The photodetection band in the long wavelength region roots in a high wavelength selective enhancement of pristine responsivity. It is worth pointing out that the largest enhancement ratio could reach up to $\sim 1200\%$ at the wavelength of 685 nm. It can be attributed to the quadrupole plasmon resonance of triangular Au NP arrays

in the visible range. Up to now, surface plasmon enhancement of photodetector by quadrupole is still lacking due to the difficult excitation of multipole resonance of metallic NPs. To get insights into the enhancement mechanism, finite difference time-domain (FDTD) simulations are performed to reveal the enhancement mechanism. The results reported in this paper provide a facile route to construct InSe-based dual-band photodetectors with high quantum efficiency and energy efficiency and lay a solid ground for the future applications of this kind of photodetector.

RESULTS AND DISCUSSION

In order to fabricate dual-band self-powered InSe photodetectors, multilayer InSe nanosheets were prepared by mechanical exfoliation method from bulk InSe crystals synthesized by Bridgeman method. To determine the phase and crystal structure of as-synthesized In_xSe_y compounds, morphologies and chemical compositions of In_xSe_y are characterized by scanning electron microscopy (SEM) and energy dispersive X-ray spectrum (EDX). As shown in Figure 1a, SEM image demonstrates that multilayer In_xSe_y is uniformly fabricated on SiO₂/Si substrate with a relatively smooth surface. EDX mapping over the In_xSe_y nanosheet demonstrated that the ratio of x and y is around 1:1.01. It is crucial to confirm the crystallographic phase of as-fabricated InSe sample owing to its influence on optoelectronic properties. In terms of the phases of InSe crystal, there are mainly three kinds of specific polytypes including β , ϵ , and γ with stacking the primitive layers in different sequences.¹⁶

The structure of InSe nanosheets was first confirmed by transmission electron microscopy (TEM) characterization. Figure 1b,c is the selected area electron diffraction (SAED) pattern and high-resolution TEM (HRTEM) image of InSe nanosheets. From the SAED pattern image, the as-fabricated InSe nanosheets have a hexagonal lattice structure with the [001] zone axis. The lattice constant along the [100] direction is 0.40 nm, d -spacing of {100} plane family is 0.34 nm, and the angle between (100) and (010) crystallographic planes is 120°. These results correspond well with the hexagonal lattice β and ϵ polytype layered InSe ($a = b = 4.05$ Å, $c = 16.93$ Å). The structural characterizations of InSe nanosheets were further

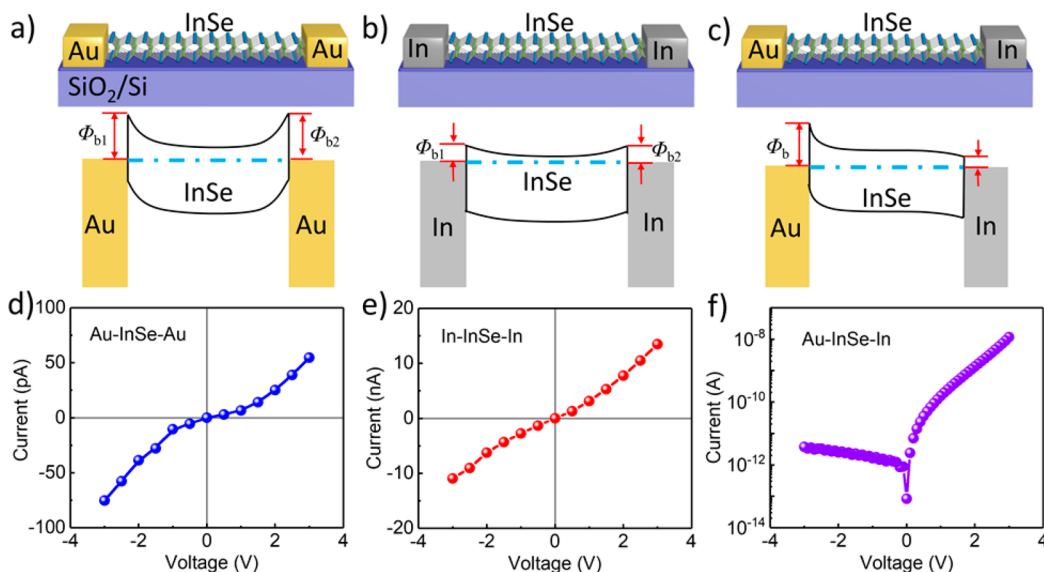


Figure 2. Design of InSe Schottky diode based on asymmetric Schottky junction. (a–c) Device structures and energy band diagrams of InSe devices with different metal contacts. (d–f) Corresponding representative I – V characteristics of InSe with different contacts, respectively.

assessed by X-ray diffraction (XRD). In Figure 1d, only five peaks at 10.8° , 21.6° , 32.5° , 43.7° , and 67.8° are observed in the XRD pattern, which can be indexed to the diffractions from (002), (004), (006), (008), and (0012) facet of hexagonal ϵ or β -InSe crystals with c -axis preferred orientation (PDF34-1431). Because the rhombohedral unit cell of γ polytype layered InSe possesses another lattice ($a = b = 4.05 \text{ \AA}$, $c = 25.32 \text{ \AA}$), the existence of γ phase could be excluded. Next, to further distinguish β and ϵ phase of InSe, Raman spectroscopy was performed to evaluate the lattice vibration modes of the InSe nanosheets from 90 to 240 cm^{-1} . As displayed in Figure 1e, three peaks at 116 , 178 , and 226 cm^{-1} are attributed to A_{1g}^1 , E_{2g}^1 and A_{2g}^2 respectively, which are consistent with the phonon mode of β -InSe.^{16,24} Therefore, the as-fabricated multilayer InSe nanosheets are confirmed to be pure β -InSe with a symmetric space group of D_{6h}^4 without any other In_xSe_y ($x \neq y$) component. To illustrate this vividly, the crystal structure of InSe nanosheets is shown in Figure 1f. Simply, β -InSe nanosheets prepared in this work are composed of several vertically stacked honeycomb lattices that consist of four covalently bonded Se-In-In-Se atomic planes, and each layer is weakly bound to its neighboring layers by van der Waals force.

The asymmetric Schottky junction was achieved by fabricating asymmetric metal contacts in this work. First, three kinds of metal-semiconductor contact conditions (Au-InSe-Au, In-InSe-In, Au-InSe-In) and their associated energy band diagrams are studied, respectively (Figure 2a–c). As is well-known, the barrier height of Schottky contact is given by the equation: $\Phi_b = \Phi - \chi$, where Φ is the work function of the metal and χ represents the electron affinity of semiconductor.²⁵ Considering the electron affinity of 4.05 eV for InSe, Au and In with work functions of 4.7 – 4.9 and $\sim 4.1 \text{ eV}$ were selected as contact metals, respectively.^{26–28} A large Schottky barrier difference would be formed between Au-InSe and In-InSe interfaces. Subsequently, the main depletion region is mainly formed on the InSe–Au interface to create a built-in electric field. When the device is under the incident light illumination, photon-generated carriers could be separated by the built-in electric field without any power supply to generate photocurrent.

Based on aforementioned analysis, several InSe-based metal-semiconductor-metal devices were fabricated on the SiO_2/Si substrate with Au and In electrodes. To explore the electrical properties of these devices, I – V curves of Au-InSe-Au, In-InSe-In, and Au-InSe-In were characterized, respectively. According to thermionic emission theory, the current I through a metal-semiconductor junction is given by²⁹

$$I = I_0 \left[\exp\left(\frac{qV}{nk_B T}\right) - 1 \right] \quad (1)$$

$$I_0 = AA^*T^2 \exp\left(\frac{-\phi_b}{k_B T}\right) \quad (2)$$

where I_0 is the reverse saturation current, n is the ideality factor, q is elementary charge, k_B is Boltzmann constant, T is absolute temperature, A is area of diode, and A^* is the effective Richardson constant. Furthermore, the eq 1 based on thermionic emission theory can be further corrected with a series resistance R and expressed as follows:^{30,31}

$$I = I_0 \left[\exp\left(\frac{qV - IR}{nk_B T}\right) - 1 \right] \quad (3)$$

Figure 2d shows the I – V plots from Au-InSe-Au contact, a lower current is found and exhibits a typical back-to-back Schottky contact properties. The Schottky barrier (Φ_b) for Au-InSe contact is around 0.673 eV which can be extracted from I – V curves (Supporting Information, Figures S1–S3). As for In-InSe contact, a larger current indicates a smaller Schottky barrier ($\Phi_b \approx 0.478 \text{ eV}$) between In and InSe due to its lower work function and more d orbital electrons, which is consistent with our results in previous work (Figure 2e).²⁶ In the case of Au-InSe-In device, the I – V curve exhibits a significant rectification characteristic with a turn-on voltage of about 1.5 V (Figure 2f), and the diode exhibits a high rectification factor of $\sim 10^3$ under $V_{\text{bias}} = 3 \text{ V}$ (11.7 nA @ 3 V ; 4.4 pA @ -3 V) with a Schottky barrier of $\sim 0.690 \text{ eV}$. Moreover, to further exclude the difference of the InSe nanosheets obtained by mechanical exfoliation method, I – V curves of another five Au-

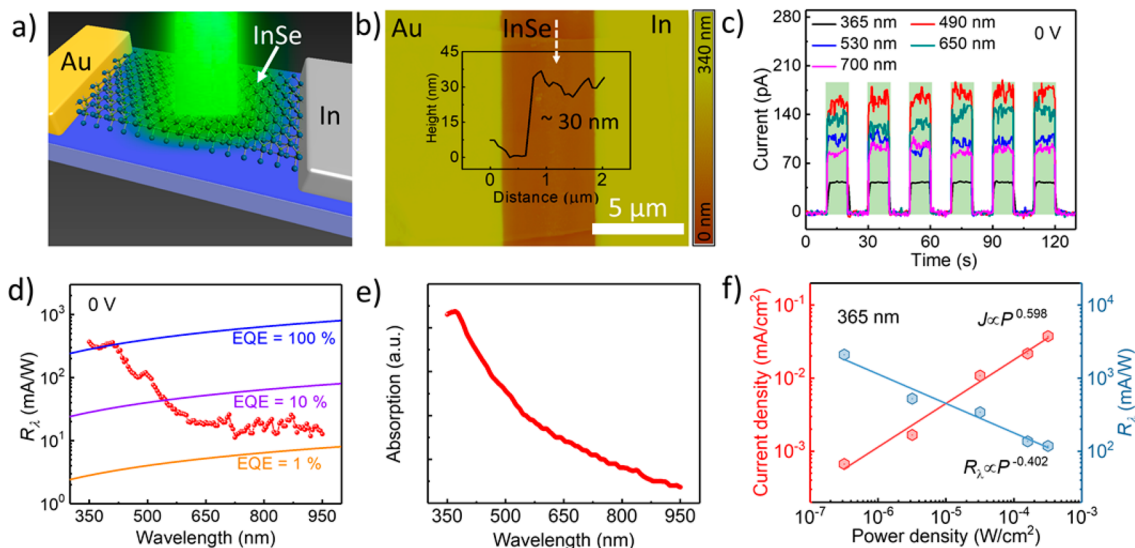


Figure 3. Optical and optoelectronic performance of InSe SPPD. (a) Schematic diagram of the device structure of pristine InSe SPPD. (b) AFM topography image of InSe SPPD and height profile along the white arrow. (c) Reproducible on/off switching of the InSe SPPD upon 365 nm (15.7 mW/cm^2), 490 nm (133 mW/cm^2), 530 nm (126 mW/cm^2), 650 nm (172 mW/cm^2), and 700 nm (131 mW/cm^2) light illumination with 0 bias voltage. (d) Spectral response of InSe SPPD ranging from 350 to 950 nm at 0 bias voltage. (e) Absorption spectrum of InSe nanosheets. (f) Photocurrent density and responsivity of InSe SPPD at the wavelength of 365 nm with the light power density ranging from 0.318 to $318 \mu\text{W}/\text{cm}^2$.

InSe-In devices were measured as well. As shown in Figure S4, they exhibit the same rectification characteristic as that in Figure 2f. The above results suggest that the InSe Schottky diode can be fabricated successfully by using Au and In electrodes, which offers additional possibilities for fabricating SPPD based on multilayer InSe nanosheets.

Figure 3a illustrates the schematic diagram of the InSe SPPD with Au and In electrodes. The device channel length is about $5 \mu\text{m}$, the light active area is about $60 \mu\text{m}^2$, and the thickness of InSe nanosheets is around 30 nm, which are confirmed by atomic force microscope (AFM) (Figure 3b). As displayed in Figure 3c, the stable and obvious photoresponse can be observed under different light illuminations, which indicates that InSe SPPD has potentiality of detecting light in UV–vis–NIR region. To further explore its working wavelength range, the spectra responsivity (Figure 3d) ranging from 350 to 950 nm was obtained critically at zero bias voltage as follows:

$$R_\lambda = \frac{I_p}{P} \quad (4)$$

where I_p is the photocurrent, which is the difference between the light current and dark current, P is the incident irradiation power, and λ is the excitation wavelength. To better understand the photoresponse properties of InSe photodetector, external quantum efficiency (EQE) measured under zero bias voltage was calculated. The EQE is a measure of the optical gain G in the photodetector. If $\text{EQE} > 1$, it means that more than one charge carrier per impinging photon is measured. The EQE of self-powered a 2D material photodetector is usually in the range of 0.1–0.2%.³² As illustrated in eq 5, EQE is the ratio of the number of charge carriers in the photocurrent n_e and the total number of impinging excitation photons n_p^t , which is closely related to the responsivity R_λ :

$$\text{EQE} = \frac{n_e}{n_p^t} = \frac{R_\lambda h c}{q \lambda} \quad (5)$$

where h is Planck's constant, c is the speed of light in vacuum, q is the elementary charge, and λ is the photon wavelength. Hence, R_λ is also plotted as a function of incident light wavelength with EQE equal to 100%, 10%, and 1%, respectively (Figure 3d). Integrated with Figure 3d and Figure S5, it can be found that EQEs of the InSe device are slightly larger than 100% in ultraviolet region ($\lambda < 400 \text{ nm}$), while EQEs decrease from 10% to 1% when the operating wavelength is in the range of 550–950 nm. Although EQEs obtained in this work are much larger than that of other 2D materials photodetectors, they are still lower than that of a conventional semiconductor photodetector at the visible and NIR region. In addition, albeit InSe should possess a cutoff edge at the wavelength of $\sim 984 \text{ nm}$ in theory, we do not observe it in experiment, and the same phenomena were also observed in previous reports.^{33,34} To further get insights into this phenomenon of InSe-based photodetector, the absorption curve of InSe nanosheets was recorded and is shown in Figure 3e. The absorption of InSe decreases dramatically as increasing of wavelength, which indicates the lower absorption coefficients in long-wavelength region of 550–950 nm. Hence, the abnormal spectral responsivity maybe arising from the intrinsic absorption properties of InSe nanosheets. To explore the reason for large EQE obtained in the short wavelength range, temporal photoresponse of the InSe self-powered photodetector was measured at the wavelength of 360 nm (Figure S6). It can be found that the decay time (75 ms) is indeed longer than that of previous works, which indicated that the large responsivity may originate from the photoconductance gain.^{35–37} At the same time, photocurrent and responsivity as a function of light intensity at the wavelength of 365 nm were measured. As shown in Figure 3f, the responsivity (R_λ) decreases nonlinearly as the illumination power (P) increases. According to previous reports, the photocurrent density (J) can be expressed by a simple power law: $J \propto P^\alpha$.^{38,39} Hence, the relationship between responsivity and power density can be given as $R_\lambda \propto P^{\alpha-1}$. Here, α is

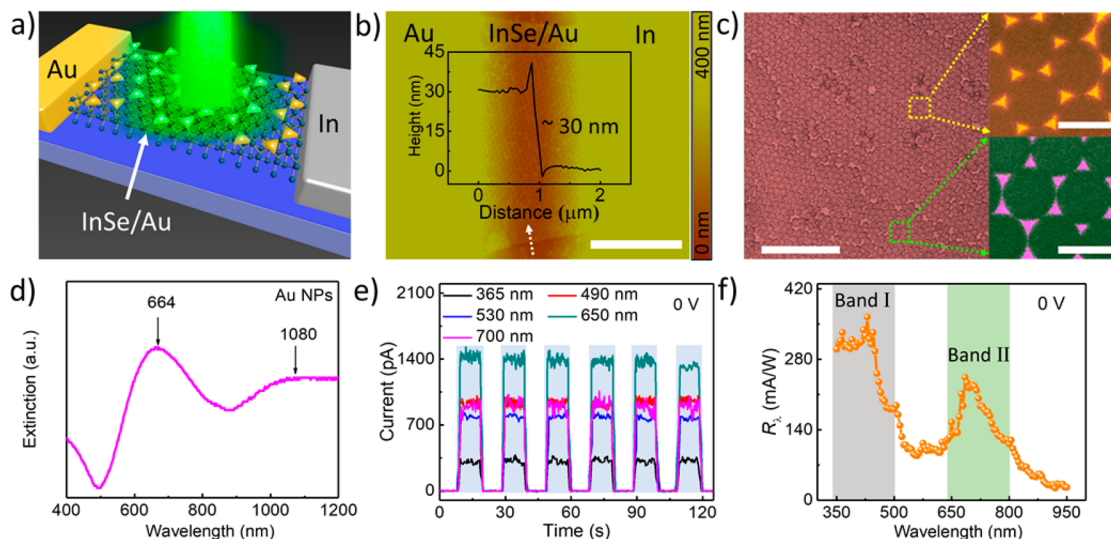


Figure 4. Plasmon-induced dual-band SPPD. (a) Schematic diagram of the device structure of InSe/Au SPPD. (b) AFM image of InSe/Au SPPD and height profile along the white arrow marks. Scale bar is 5 μm . (c) SEM images of Au NPs on SiO_2/Si substrate, the scale bars are 5 μm and 500 nm in left and right inset image. (d) Extinction spectrum of Au NPs at wavelength of 400–1200 nm. (e) Reproducible on/off switching of the InSe/Au SPPD with the same test conditions in Figure 3c. (f) Responsivity of InSe/Au SPPD at 0 bias voltage.

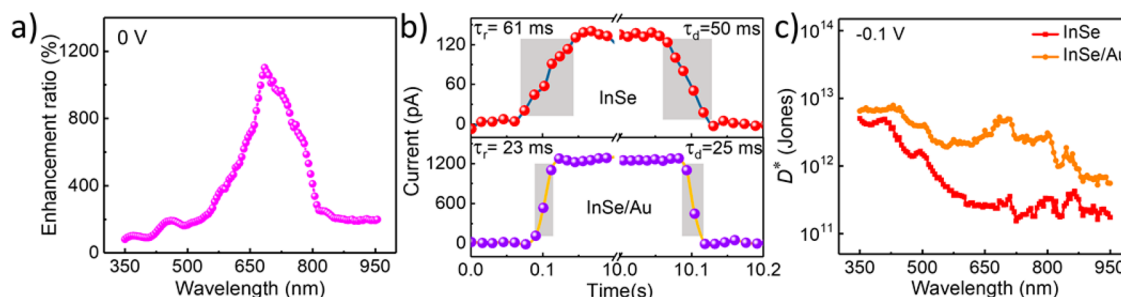


Figure 5. Surface plasmons enhancement of InSe SPPD by Au NPs patterning arrays. (a) Responsivity selectively enhancement of InSe SPPD via surface plasmon resonance with illumination wavelength ranging from 350 to 950 nm. (b) Time resolved photoresponse of InSe and InSe/Au SPPD upon 685 nm light illumination at 0 V. (c) Detectivities of InSe and InSe/Au SPPD at -0.1 V.

calculated to be ~ 0.598 with the illumination power density ranging from $3.18 \times 10^{-7} \text{ W/cm}^2$ to $3.18 \times 10^{-4} \text{ W/cm}^2$, suggesting a complex process of electron–hole generation, recombination, and trapping in our device. Therefore, schemes are greatly needed for extending photodetection ability of pristine InSe SPPD to the long wavelength region.

Surface plasmon resonance is a kind of hybrid electromagnetic wave arising from the collective oscillations of free electron gas within metal, which possesses the ability of manipulating light at nanoscale with a high local-field enhancement.^{22,40–42} This makes it possible to improve the photoelectric conversion efficiency of a photodetector at the resonance wavelength.^{21,43–45} Based on this theory, InSe/Au SPPD was designed by patterning triangular Au NP arrays onto the surface of InSe nanosheets (Figure 4a). According to AFM image in Figure 4b, the hexagonal arrangement of Au NPs is formed well on the surface of InSe nanosheets, and the channel length and thickness of InSe flake are same as that of pristine InSe device (Figure 3d). From the SEM images in Figure 4c, the triangular Au NP arrays are hexagonal patterned, with side lengths of single triangular Au NPs ranging from 70 to 250 nm (Figure S7), and their thickness is ~ 25 nm (Figure S8). As shown in Figure 4d, their extinction spectrum exhibits two peaks clearly: one is located at visible range (664 nm), and the other is located at NIR range (1080 nm). Notably, an

asymmetric profile was observed in the short wavelength, which is well-known as a Fano-like profile. According to our and others' previous work, the special profiles in extinction spectra could be mainly attributed to the coupling interaction between dipole and quadrupole of triangular Au NPs arrays.^{46–48}

To examine Au plasmonic enhancement effects of InSe photodetector preliminarily, the on/off switching currents of InSe/Au device at different wavelengths were recorded under zero bias voltage at first (Figure 4e). Under identical test conditions, all photocurrents of InSe/Au SPPD were improved significantly compared with that of pristine InSe SPPD (Figure 3c). Then, to demonstrate the enhancement effect of photocurrents vividly, spectral responsivity of InSe/Au SPPD ranging from 350 to 950 nm was characterized. As shown in Figure 4f, unlike pristine InSe SPPD which can only operate in UV–vis short wavelength regime (Figure 3d), InSe/Au SPPD exhibits a dual-band photodetection in UV–vis-NIR broadband region. In conjunction with the extinction of the trigonal Au NPs, additional photodetection of InSe/Au SPPD in the visible region may be induced by surface plasmon resonance. To further confirm this conjecture, linear dynamic range properties (LDR, typically quoted in dB) of InSe photodetector with and without Au NPs were analyzed at zero bias voltage. Generally, LDR can be obtained from the equation:

$$\text{LDR} = 20 \log_{10} \left(\frac{I_p}{I_d} \right) \quad (6)$$

where I_p is the photocurrent, and I_d is the dark current. Compared with pristine InSe SPPD, LDR of InSe/Au device is enhanced remarkably, especially in the visible region as well (Figure S9). As an example, LDR is enhanced from 43 to 64 dB at the wavelength of 650 nm, which is comparable to that of InGaAs-based photodetectors (66 dB).⁴⁹

Subsequently, enhancement ratios of responsivity as a function of the wavelength were explored (Figure 5a). It can be found that responsivities of InSe SPPD are very large in the visible region and they are strongly dependent on the wavelength over a broadband ranging from UV to NIR regions. However, the enhancement ratio does not increase monotonically as wavelength increases. For example, the enhanced ratio of responsivity is ~103% at the wavelength of 365 nm, while it could reach up to a peak value of ~1200% at the wavelength of 685 nm (Figure 5a). More interestingly, EQE enhanced trend (Figures S5 and S10) corresponds well with the extinction spectrum of triangular Au NP arrays (Figure 4d). To further confirm that the high wavelength selective enhancement of responsivity originates from the quadrupole plasmons of Au NPs, response times of SPPDs with and without Au NPs were investigated at the wavelength of 685 nm. As shown in Figure 5b, the response time can be decreased largely after bringing in Au NPs arrays on the surface of InSe nanosheets. This may arise from the effective surface plasmon-exciton coupling process.^{50,51} In addition, another five SPPDs with and without Au NPs were fabricated and characterized by the same process mentioned above, and the similar selective enhancement trend (Figure S11) indicates that the strategy proposed herein for fabricating dual-band SPPDs is highly reliable and reproducible. Another important figure of merit for a photodetector is detectivity (D^*), which usually describes the smallest detectable signal. As the shot noise is considered as the major component in total noise, the detectivity (D^*) could be expressed as⁵²

$$D^* = \frac{\sqrt{AB}}{\text{NEP}} \approx \frac{R_\lambda}{\sqrt{\frac{2qI_d}{A}}} \quad (7)$$

where B is the bandwidth, q is the elemental charge, I_d is the dark current, A is active area ($\sim 60 \mu\text{m}^2$), and R_λ is the responsivity. The calculated detectivity D^* in the range from 350 to 950 nm under a low bias voltage (-0.1 V) of both two devices was plotted in Figure 5c. It can be found that the enhanced trend of D^* is same as that of EQE and responsivity. Only one large enhancement of D^* is obtained in the visible regime as well, especially at the wavelength of 685 nm, which could be enhanced by one order from 2.56×10^{11} to 3.35×10^{12} Jones. This demonstrates that D^* of InSe SPPD could be comparable to that of traditional photodetectors in the visible region after patterning Au NPs arrays on the surface of InSe nanosheets.

To shed light on the origin of plasmon resonance and the mechanism of dual-band responsivity induced by triangular Au NPs patterning arrays, we systematically simulated the extinction spectra (scattering and absorption) of Au NPs with different size and distributions by FDTD method. In the following simulations, the optical constants of Au NPs were measured by Johnson and Christy, and InSe was considered in our calculations.⁵³ As is well-known, the spectral shape and

position of the extinction in metallic NPs are highly sensitive to their size, shape, and internal gap.⁵⁴

To simplify the models, the extinction spectra of isolated triangular Au NPs were calculated. Based on our experimental results, isolated triangular Au NPs with sizes ranging from 70 to 140 nm (Figure S7) and thickness of ~25 nm (Figure S8) were considered. As shown in Figure 6a, the red shift of

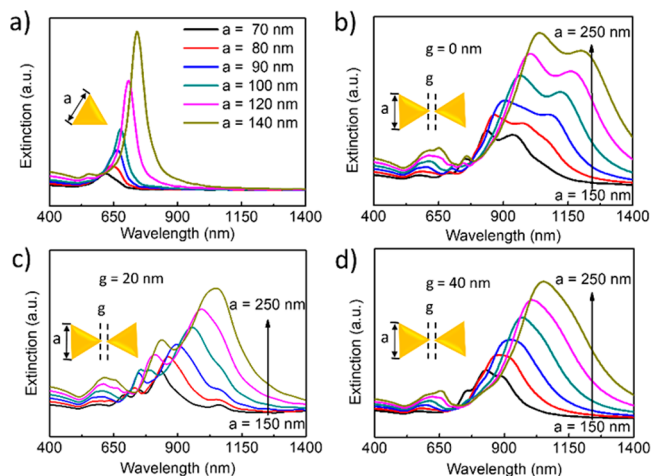


Figure 6. Extinction spectra of triangular Au NPs obtained by FDTD simulation. (a) Extinction spectra of isolated Au NP with lateral sizes (a) of 70, 80, 90, 100, 120, and 140 nm. (b–d) Extinction spectra of Au NPs homodimers with interspace gap (g) of 0, 20, 40 nm and with their lateral sizes ranging from 150 to 250 nm with 20 nm increment.

plasmon resonance peaks is found with an increase in the slide length of triangular Au NPs, and all peak wavelengths of extinction spectra exhibit in the visible region from ~610 to ~740 nm. Besides the dipole modes, quadrupole resonance peak can be clearly observed when the lateral size is larger than 80 nm. Moreover, with the increase of triangular Au NPs, the quadrupole resonance intensity becomes stronger. These results indicate that the high order surface plasmon resonance modes could occur in the isolated triangular Au NPs with relatively large size due to the inhomogeneous distribution of electron density.⁵⁵

Considering the inhomogeneous dispersion of triangular Au NPs in our experiment (Figure 4c and Figure S7, S8), the interaction among the triangular NPs could not be ignored, which would affect the resonance position of extinction spectrum. Subsequently, the extinction spectra of triangular Au homodimer with various interspace gaps ($g = 0, 20, 40$ nm) are carried out. It can be found that all extinction spectra exhibit two peaks (Figure 6b–d). With the increase of average size of homodimer, the dipole peak presents an obvious red-shift, while the quadrupole peak only showed a slight red-shift. In addition, the intensity and shape of both dipole and quadrupole resonances could be tailored by tuning the distance of triangular Au NPs. And the spectral position of surface plasmon resonance is just located at visible and NIR regions which is consistent with the extinction spectrum in our experimental results (Figure 4d).

A simple dimer in the simulation could not directly describe the inhomogeneous triangular Au NPs patterning arrays in our experiment, and the interaction of dimers with each other could not be excluded completely. To simplify the models,

simulated extinction spectra of coupling interaction among inhomogeneous dispersion of Au NPs are not provided herein. Therefore, the intensity of two peaks in our experimental extinction spectrum may be different from idealized simulation curves. However, it does not affect the understanding the original extinction spectrum of our inhomogeneous Au NPs. Considering the coupling interactions among Au NPs, two peaks in our experimental extinction spectrum are hybrid quadrupole and hybrid dipole, which are induced by large size, asymmetric architecture, and the coupling interactions of Au NPs. In this case, these two modes in triangular Au NPs can be both actively excited. Because dipole plasmon resonance of Au NPs is located in the NIR region which is close to the cutoff wavelength of InSe photodetector, only one giant enhancement peak of EQE is obtained in the visible region. This is induced by Au NPs based on the coupling interaction between the hybridized quadrupole plasmons in Au NP aggregation and the excitons InSe nanosheets. Therefore, in conjunction with the pristine photodetection band in the short wavelength, InSe/Au SPPD possesses the capability of dual-band photodetection.

CONCLUSIONS

In summary, a dual-band InSe/Au SPPD based on surface plasmon resonance and asymmetric Schottky junction was proposed in this work. Albeit the responsivity of pristine InSe device decays significantly in the long wavelength range, after covering plasmonic Au NPs patterning arrays on the surface of InSe nanosheet, the aperiodic responsivity of InSe/Au SPPDs could exhibit dual-band response both in UV-vis and visible-NIR regions. Two peak responsivities of the dual-band SPPDs could reach up to 369 and 244 mA/W at the wavelengths of 365 and 685 nm under zero bias voltage, which are much higher than that of previous SPPDs (Figure S12). In particular, the enhancement ratio could reach up to ~1200% at the wavelength of 685 nm. LDR of the device could be enhanced from 43 to 64 dB at the wavelength of 650 nm, which is comparable to that of InGaAs-based photodetectors (66 dB). D^* of the device could be enhanced by one order from $\sim 10^{11}$ to $\sim 10^{12}$ Jones, which is comparable to that of previous SPPDs based on 2D materials (Figure S12). Our approach provides a facile route to fabricate multiband SPPDs, and this work may also lay a solid ground for the future applications of multipole surface plasmon resonances in the further development of optoelectronic devices.

METHODS

Fabrication of InSe Nanosheets by Bridgeman and Mechanical Exfoliation Method. Bulk InSe crystals were prepared by following procedure. First, selenium powder and indium particles with mole ratio of 1:1.1 were put into a quartz boat. Then, the boat was put into a horizontal furnace with a fused silica tube. The closing system was purged with 500 sccm Ar gas for 20 min. Next, the boat with In and Se was heated to 573 K and kept for 30 min with 13/7 sccm Ar/H₂ mixed gas. After that, the boat was heated up to a higher temperature of 933 K for 1 h. Ultimately, the system was allowed to cool-down to room temperature naturally. Before mechanical exfoliation of InSe nanosheets from bulk InSe crystals, SiO₂/Si substrate was pretreated with standard piranha solution (H₂SO₄:H₂O₂ with volume ratio of 7:3) and ultrasonic cleaned for 10 min with isopropanol, acetone, ethanol, and deionized water, respectively. Then, a piece of InSe flake was put onto Scotch tape (Scotch 3M) and was pasted repeatedly. Subsequently, the Scotch tape was pasted to

the SiO₂/Si substrate and kept for 6 h at least. Then, InSe nanosheets were prepared on SiO₂/Si substrate after removing the Scotch tape.

Synthesis and Transfer of Au Triangular Nanoarrays. Au NPs are prepared by a conventional nanosphere lithography method. First, the silica (SiO₂) nanospheres as the unit of shadow mask were synthesized as in previous reports.^{56,57} Then, the prepared SiO₂ spheres with average diameters of 450 nm were monodispersed in water–ethanol mixed solvent. Subsequently, the monolayer SiO₂ sphere arrays film was scooped by a SiO₂/Si substrate and baked at 70 °C for 30 min. Then a gold thin film 25 nm thick was deposited by thermal evaporation. After that, the SiO₂ sphere array film was removed by tape, and the patterned triangular Au NP arrays were prepared on the substrate.

The as-synthesized Au NPs were transferred to an InSe nanosheet assisted with poly(methyl methacrylate) (PMMA). The Au NPs were covered with a PMMA film by spin coating, followed by baking at 130 °C for 20 min. After removing the SiO₂/Si substrate by HF solution, the PMMA/Au NPs stack was transferred onto a target InSe nanosheet. Finally, PMMA film was removed by acetone.

Fabrication of InSe and InSe/Au Photodetectors. First, Au and In electrodes 50 nm thick were fabricated on the InSe nanosheets with and without Au NPs arrays using thermal evaporation with a shadow mask, respectively. All devices were annealed under 200 °C for 30 min in Ar/H₂ (90/10 sccm) atmosphere before electrical measurements. Lastly, the devices were packaged by polydimethylsiloxane (PDMS) to protect electrodes and InSe nanosheets from oxidation in air.

Characterizations. Morphologies of the sample were characterized using SEM (Hitachi S-4200) and AFM (Bruker Dimension Icon). EDX was used to determine the composition of InSe nanosheets. The structure characteristics of InSe nanosheets is studied using a Raman spectroscopy (LabRAM XploRA, laser wavelength is 532 nm). The structure of samples was identified by XRD (DIFFRACTOMETER-6000) and TEM (Tecnai-G2 F30). The optical properties of InSe and Au NPs were investigated by optical diffuse absorption spectra using a UV-vis spectrophotometer (Hitachi U-4100). The electrical and optoelectronic performances were analyzed with a xenon lamp, monochromator (Zolix, Omni-λ300i), a program-controlled semiconductor characterization system (Keithley 4200-PA SCS), and a probe station (Lakeshore), respectively.

ASSOCIATED CONTENT

S Supporting Information

The Supporting Information is available free of charge on the ACS Publications website at DOI: [10.1021/acsnano.8b04931](https://doi.org/10.1021/acsnano.8b04931).

Calculation and Characterization details with corresponding figures ([PDF](#))

AUTHOR INFORMATION

Corresponding Authors

*E-mail: chenhy@hit.edu.cn.

*E-mail: hupa@hit.edu.cn.

ORCID ®

Mingjin Dai: [0000-0001-6009-1715](https://orcid.org/0000-0001-6009-1715)

Wei Feng: [0000-0001-6902-0024](https://orcid.org/0000-0001-6902-0024)

Jia Zhang: [0000-0003-0943-7543](https://orcid.org/0000-0003-0943-7543)

Cheng-Yan Xu: [0000-0002-7835-6635](https://orcid.org/0000-0002-7835-6635)

PingAn Hu: [0000-0003-3499-2733](https://orcid.org/0000-0003-3499-2733)

Notes

The authors declare no competing financial interest.

ACKNOWLEDGMENTS

We would like to thank Prof. Lin Li for his kind help. This work is supported by the National Natural Science Foundation

of China (61390502 and 61505033), Foundation for Innovative Research Groups of the National Natural Science Foundation of China (51521003), National Postdoctoral Science Foundation of China (2017M621254 and 2018T110280), Heilongjiang Provincial Postdoctoral Science Foundation (LBH-TZ1708), Self-Planned Task (SKLRS201607B) of State Key Laboratory of Robotics and System (HIT), and Key Laboratory of Microsystems and Microstructures Manufacturing of Ministry of Education, Harbin Institute of Technology (2017KM003).

REFERENCES

- (1) Wang, P.; Liu, S. S.; Luo, W. J.; Fang, H. H.; Gong, F.; Guo, N.; Chen, Z. G.; Zou, J.; Huang, Y.; Zhou, X. H.; Wang, J. L.; Chen, X. S.; Lu, W.; Xiu, F. X.; Hu, W. D. Arrayed van der Waals Broadband Detectors for Dual-Band Detection. *Adv. Mater.* **2017**, *29*, 1604439.
- (2) Lefler, S.; Vizel, R.; Yeor, E.; Granot, E.; Heifler, O.; Kwiat, M.; Krivitsky, V.; Weil, M.; Yaish, Y. E.; Patolsky, F. Multicolor Spectral-Specific Silicon Nanodetectors Based on Molecularly Embedded Nanowires. *Nano Lett.* **2018**, *18*, 190–201.
- (3) Plis, E. A.; Gautam, N.; Kutty, M. N.; Myers, S.; Klein, B.; Schuler-Sandy, T.; Naydenkov, M.; Krishna, S. Performance of Long-Wave Infrared InAs/GaSb Strained Layer Superlattice Detectors for the Space Applications. *Proc. SPIE* **2011**, 81640S.
- (4) Peng, L.; Hu, L. F.; Fang, X. S. Energy Harvesting for Nanostructured Self-Powered Photodetectors. *Adv. Funct. Mater.* **2014**, *24*, 2591–2610.
- (5) Chen, H. Y.; Liu, K. W.; Hu, L. F.; Al-Ghamdi, A. A.; Fang, X. S. New Concept Ultraviolet Photodetectors. *Mater. Today* **2015**, *18*, 493–502.
- (6) Chen, H. Y.; Liu, K. W.; Chen, X.; Zhang, Z. Z.; Fan, M. M.; Jiang, M. M.; Xie, X. H.; Zhao, H. F.; Shen, D. Z. Realization of a Self-Powered ZnO MSM UV Photodetector with High Responsivity Using an Asymmetric Pair of Au Electrodes. *J. Mater. Chem. C* **2014**, *2*, 9689–9694.
- (7) Hatch, S. M.; Briscoe, J.; Dunn, S. A Self-Powered ZnO-Nanorod/CuSCN UV Photodetector Exhibiting Rapid Response. *Adv. Mater.* **2013**, *25*, 867–871.
- (8) Xie, X. H.; Zhang, Z. Z.; Shan, C. X.; Chen, H. Y.; Shen, D. Z. Dual-Color Ultraviolet Photodetector Based on Mixed-Phase-MgZnO/i-MgO/p-Si Double Heterojunction. *Appl. Phys. Lett.* **2012**, *101*, 081104.
- (9) Hoang, A. M.; Dehzangi, A.; Adhikary, S.; Razeghi, M. High Performance Bias-Selectable Three-Color Short-Wave/Mid-Wave/Long-Wave Infrared Photodetectors Based on Type-II InAs/GaSb/AlSb Superlattices. *Sci. Rep.* **2016**, *6*, 24144.
- (10) Dupont, E.; Gao, M.; Wasilewski, Z.; Liu, H. C. Integration of N-type and P-type Quantum-Well Infrared Photodetectors for Sequential Multicolor Operation. *Appl. Phys. Lett.* **2001**, *78*, 2067–2069.
- (11) Su, L. X.; Chen, H. Y.; Xu, X. J.; Fang, X. S. Novel BeZnO Based Self-Powered Dual-Color UV Photodetector Realized via a One-Step Fabrication Method. *Laser Photonics Rev.* **2017**, *11*, 1700222.
- (12) Wang, S. S.; Wang, X. C.; Warner, J. H. All Chemical Vapor Deposition Growth of MoS₂:h-BN Vertical van der Waals Heterostructures. *ACS Nano* **2015**, *9*, 5246–5254.
- (13) Ahn, G. H.; Amani, M.; Rasool, H.; Lien, D. H.; Mastandrea, J. P.; Ager, J. W., III; Dubey, M.; Chrzan, D. C.; Minor, A. M.; Javey, A. Strain-engineered Growth of Two-Dimensional Materials. *Nat. Commun.* **2017**, *8*, 608.
- (14) Yi, Y.; Yu, X. F.; Zhou, W. H.; Wang, J. H.; Chu, P. K. Two-Dimensional Black Phosphorus: Synthesis, Modification, Properties, and Applications. *Mater. Sci. Eng., R* **2017**, *120*, 1–33.
- (15) Medina, H.; Li, J. G.; Su, T. Y.; Lan, Y. W.; Lee, S. H.; Chen, C. W.; Chen, Y. Z.; Manikandan, A.; Tsai, S. H.; Navabi, A.; Zhu, X. D.; Shih, Y. C.; Lin, W. S.; Yang, J. H.; Thomas, S. R.; Wu, B. W.; Shen, C. H.; Shieh, J. M.; Lin, H. N.; Javey, A.; Wang, K. L.; Chueh, Y. L. Wafer-Scale Growth of WSe₂ Monolayers Toward Phase-Engineered Hybrid WO_x/WSe₂ Films with Sub-ppb NO_x Gas Sensing by a Low-Temperature Plasma-Assisted Selenization Process. *Chem. Mater.* **2017**, *29*, 1587–1598.
- (16) Yang, Z. B.; Jie, W. J.; Mak, C. H.; Lin, S. H.; Lin, H. H.; Yang, X. F.; Yan, F.; Lau, S. P.; Hao, J. H. Wafer-Scale Synthesis of High-Quality Semiconducting Two-Dimensional Layered InSe with Broadband Photoresponse. *ACS Nano* **2017**, *11*, 4225–4236.
- (17) Feng, W.; Zheng, W.; Cao, W. W.; Hu, P. A. Back Gated Multilayer InSe Transistors with Enhanced Carrier Mobilities via the Suppression of Carrier Scattering from a Dielectric Interface. *Adv. Mater.* **2014**, *26*, 6587–6593.
- (18) Feng, W.; Wu, J. B.; Li, X. L.; Zheng, W.; Zhou, X.; Xiao, K.; Cao, W. W.; Yang, B.; Idrobo, J. C.; Basile, L.; Tian, W. Q.; Tan, P. H.; Hu, P. A. Ultrahigh Photo-Responsivity and Detectivity in Multilayer InSe Nanosheets Phototransistors with Broadband Response. *J. Mater. Chem. C* **2015**, *3*, 7022–7028.
- (19) Makkawi, O.; Qiu, Y. F.; Feng, W.; Hu, P. A. The Modulation of Photoluminescence Band Gap of Two-Dimensional InSe Nanosheets on h-BN Substrate. *J. Nanosci. Nanotechnol.* **2016**, *16*, 9813–9819.
- (20) Lei, S. D.; Wen, F. F.; Ge, L. H.; Najmaei, S.; George, A.; Gong, Y. J.; Gao, W. L.; Jin, Z. H.; Li, B.; Lou, J.; Kono, J.; Vajtai, R.; Ajayan, P.; Halas, N. J. An Atomically Layered InSe Avalanche Photodetector. *Nano Lett.* **2015**, *15*, 3048–3055.
- (21) Hu, K.; Chen, H. Y.; Jiang, M. M.; Teng, F.; Zheng, L. X.; Fang, X. S. Broadband Photoresponse Enhancement of a High-Performance t-Se Microtube Photodetector by Plasmonic Metallic Nanoparticles. *Adv. Funct. Mater.* **2016**, *26*, 6641–6648.
- (22) Hwang, S. W.; Shin, D. H.; Kim, C. O.; Hong, S. H.; Kim, M. C.; Kim, J.; Lim, K. Y.; Kim, S.; Choi, S. H.; Ahn, K. J.; Kim, G.; Sim, S. H.; Hong, B. H. Plasmon-Enhanced Ultraviolet Photoluminescence from Hybrid Structures of Graphene/ZnO Films. *Phys. Rev. Lett.* **2010**, *105*, 127403.
- (23) Chen, Z. F.; Li, X. M.; Wang, J. Q.; Tao, L.; Long, M. Z.; Liang, S. J.; Ang, L. K.; Shu, C.; Tsang, H. K.; Xu, J. B. Synergistic Effects of Plasmonics and Electron Trapping in Graphene Short-Wave Infrared Photodetectors with Ultrahigh Responsivity. *ACS Nano* **2017**, *11*, 430–437.
- (24) Lei, S. D.; Ge, L. H.; Najmaei, S.; George, A.; Kappera, R.; Lou, J.; Chhowalla, M.; Yamaguchi, H.; Gupta, G.; Vajtai, R.; Mohite, A. D.; Ajayan, P. M. Evolution of the Electronic Band Structure and Efficient Photo-Detection in Atomic Layers of InSe. *ACS Nano* **2014**, *8*, 1263–1272.
- (25) Leonard, F.; Talin, A. A. Electrical Contacts to One- and Two-Dimensional Nanomaterials. *Nat. Nanotechnol.* **2011**, *6*, 773–783.
- (26) Feng, W.; Zhou, X.; Tian, W. Q.; Zheng, W.; Hu, P. A. Performance Improvement of Multilayer InSe Transistors with Optimized Metal Contacts. *Phys. Chem. Chem. Phys.* **2015**, *17*, 3653–3658.
- (27) Hansen, W. N.; Johnson, K. B. Work Function Measurements in Gas Ambient. *Surf. Sci.* **1994**, *316*, 373–382.
- (28) Helander, M. G.; Greiner, M. T.; Wang, Z. B.; Lu, Z. H. Pitfalls in measuring work function using photoelectron spectroscopy. *Appl. Surf. Sci.* **2010**, *256*, 2602–2605.
- (29) Lee, S.; Tang, A.; Aloni, S.; Wong, H. S. P. Statistical Study on the Schottky Barrier Reduction of Tunneling Contacts to CVD Synthesized MoS₂. *Nano Lett.* **2016**, *16*, 276–281.
- (30) Di Bartolomeo, A.; Luongo, G.; Giubileo, F.; Funicello, N.; Niu, G.; Schroeder, T.; Lisker, M.; Lupina, G. Hybrid Graphene/Silicon Schottky Photodiode with Intrinsic Gating Effect. *2D Mater.* **2017**, *4*, 025075.
- (31) Osvald, J. Back-to-Back Connected Asymmetric Schottky Diodes with Series Resistance as a Single Diode. *Phys. Status Solidi A* **2015**, *212*, 2754–2758.
- (32) Buscema, M.; Island, J. O.; Groenendijk, D. J.; Blanter, S. I.; Steele, G. A.; van der Zant, H. S. J.; Castellanos-Gomez, A. Photocurrent Generation with Two-Dimensional van der Waals Semiconductors. *Chem. Soc. Rev.* **2015**, *44*, 3691–3718.

- (33) Kyazym-Zade, A. G.; Salmanov, V. M.; Guseinov, A. G.; Mamedov, R. M.; Salmanova, A. A.; Akhmedova, F. Sh. Special Features of the Optical Absorption and Photoconductivity of Indium Monoselenide Upon Laser Excitation. *Russ. Phys. J.* **2018**, *60*, 1680–1683.
- (34) Yang, S.; Kelley, D. F. The Spectroscopy of InSe Nanoparticles. *J. Phys. Chem. B* **2005**, *109*, 12701–12709.
- (35) Feng, W.; Jin, Z.; Yuan, J.; Zhang, J.; Jia, S.; Dong, L.; Yoon, J.; Zhou, L.; Vajtai, R.; Tour, J. M.; Ajayan, P. M.; Hu, P.; Lou, J. A Fast and Zero-Biased Photodetector Based on GaTe-InSe Vertical 2D p-n Heterojunction. *2D Mater.* **2018**, *5*, 025008.
- (36) Yan, F. G.; Zhao, L. X.; Patane, A. L.; Hu, P. A.; Wei, X.; Luo, W. G.; Zhang, D.; Lv, Q. S.; Feng, Q.; Shen, C.; Chang, K.; Eaves, L.; Wang, K. Y. Fast, Multicolor Photodetection with Graphene-Contacted p-GaSe/n-InSe van der Waals Heterostructures. *Nanotechnology* **2017**, *28*, 27LT01.
- (37) Chen, H. Y.; Liu, H.; Zhang, Z. M.; Hu, K.; Fang, X. S. Nanostructured Photodetectors: From Ultraviolet to Terahertz. *Adv. Mater.* **2016**, *28*, 403–433.
- (38) Chen, Y.; Wang, X. D.; Wu, G. J.; Wang, Z.; Fang, H. H.; Lin, T.; Sun, S.; Shen, H.; Hu, W. D.; Wang, J. L.; Sun, J. L.; Meng, X. J.; Chu, J. H. High-Performance Photovoltaic Detector Based on MoTe₂/MoS₂ Van der Waals Heterostructure. *Small* **2018**, *14*, 1703293.
- (39) Kind, H.; Yan, H. Q.; Messer, B.; Law, M.; Yang, P. D. Nanowire Ultraviolet Photodetectors and Optical Switches. *Adv. Mater.* **2002**, *14*, 158–160.
- (40) Dong, L. L.; Yang, X.; Zhang, C.; Cerjan, B.; Zhou, L. N.; Tseng, M. L.; Zhang, Y.; Alabastri, A.; Nordlander, P.; Halas, N. J. Nanogapped Au Antennas for Ultrasensitive Surface-Enhanced Infrared Absorption Spectroscopy. *Nano Lett.* **2017**, *17*, 5768–5774.
- (41) Tseng, M. L.; Yang, J.; Semmlinger, M.; Zhang, C.; Nordlander, P.; Halas, N. J. Two-Dimensional Active Tuning of an Aluminum Plasmonic Array for Full-Spectrum Response. *Nano Lett.* **2017**, *17*, 6034–6039.
- (42) Atwater, H. A.; Polman, A. Plasmonics for Improved Photovoltaic Devices. *Nat. Mater.* **2010**, *9*, 205–213.
- (43) Petoukhoff, C. E.; Krishna, M. B. M.; Voiry, D.; Bozkurt, I.; Deckoff-Jones, S.; Chhowalla, M.; O'Carroll, D. M.; Dani, K. M. Ultrafast Charge Transfer and Enhanced Absorption in MoS₂-Organic van der Waals Heterojunctions Using Plasmonic Metasurfaces. *ACS Nano* **2016**, *10*, 9899–9908.
- (44) Chen, Z. F.; Li, X. M.; Wang, J. Q.; Tao, L.; Long, M. Z.; Liang, S. J.; Ang, L. K.; Shu, C.; Tsang, H. K.; Xu, J. B. Synergistic Effects of Plasmonics and Electron Trapping in Graphene Short-Wave Infrared Photodetectors with Ultrahigh Responsivity. *ACS Nano* **2017**, *11*, 430–437.
- (45) Greybush, N. J.; Liberal, I.; Malassis, L.; Kikkawa, J. M.; Engheta, N.; Murray, C. B.; Kagan, C. R. Plasmon Resonances in Self-Assembled Two-Dimensional Au Nanocrystal Metamolecules. *ACS Nano* **2017**, *11*, 2917–2927.
- (46) Chen, H. Y.; Liu, K. W.; Jiang, M. M.; Zhang, Z. Z.; Xie, X. H.; Wang, D. K.; Liu, L.; Li, B. H.; Zhao, D. X.; Shan, C. X.; Shen, D. Z. Tunable Enhancement of Exciton Emission from MgZnO by Hybridized Quadrupole Plasmons in Ag Nanoparticle Aggregation. *Appl. Phys. Lett.* **2014**, *104*, 091119.
- (47) Jiang, M. M.; Chen, H. Y.; Li, B. H.; Liu, K. W.; Shan, C. X.; Shen, D. Z. Hybrid Quadrupolar Resonances Stimulated at Short Wavelengths Using Coupled Plasmonic Silver Nanoparticle Aggregation. *J. Mater. Chem. C* **2014**, *2*, 56–63.
- (48) Chen, H. Y.; Liu, K. W.; Jiang, M. M.; Zhang, Z. Z.; Liu, L.; Li, B. H.; Xie, X. H.; Wang, F.; Zhao, D. X.; Shan, C. X.; Shen, D. Z. Tunable Hybridized Quadrupole Plasmons and Their Coupling with Excitons in ZnMgO/Ag System. *J. Phys. Chem. C* **2014**, *118*, 679–684.
- (49) Liu, S.; Wei, Z. M.; Cao, Y.; Gan, L.; Wang, Z. X.; Xu, W.; Guo, X. F.; Zhu, D. B. Ultrasensitive Water-Processed Monolayer Photodetectors. *Chem. Sci.* **2011**, *2*, 796–802.
- (50) Okamoto, K.; Niki, I.; Shvartser, A.; Narukawa, Y.; Mukai, T.; Scherer, A. Surface-Plasmon-Enhanced Light Emitters Based on InGaN Quantum Wells. *Nat. Mater.* **2004**, *3*, 601–605.
- (51) Zang, Y. S.; He, X.; Li, J.; Yin, J.; Li, K. Y.; Yue, C.; Wu, Z. M.; Wu, S. T.; Kang, J. Y. Band Edge Emission Enhancement by Quadrupole Surface Plasmon-Exciton Coupling Using Direct-Contact Ag/ZnO Nanospheres. *Nanoscale* **2013**, *5*, 574–580.
- (52) Chen, Y.; Wang, X.; Wu, G.; Wang, Z.; Fang, H.; Lin, T.; Sun, S.; Shen, H.; Hu, W.; Wang, J.; Sun, J.; Meng, X.; Chu, J. High-Performance Photovoltaic Detector Based on MoTe₂/MoS₂ van der Waals Heterostructure. *Small* **2018**, *14*, 1703293.
- (53) Johnson, P. B.; Christy, R. W. Optical Constants of the Noble Metals. *Phys. Rev. B* **1972**, *6*, 4370–4379.
- (54) Linic, S.; Christopher, P.; Ingram, D. B. Plasmonic-Metal Nanostructures for Efficient Conversion of Solar to Chemical Energy. *Nat. Mater.* **2011**, *10*, 911.
- (55) Noguez, C. Surface Plasmons on Metal Nanoparticles: The Influence of Shape and Physical Environment. *J. Phys. Chem. C* **2007**, *111*, 3806–3819.
- (56) Lin, C. N.; Huang, M. H. Formation of Hollow Gallium Nitride Spheres via Silica Sphere Templates. *J. Phys. Chem. C* **2009**, *113*, 925–929.
- (57) Zhang, T. R.; Zhang, Q.; Ge, J. P.; Goebel, J.; Sun, M. W.; Yan, Y. S.; Liu, Y. S.; Chang, C. L.; Guo, J. H.; Yin, Y. D. A Self-Templated Route to Hollow Silica Microspheres. *J. Phys. Chem. C* **2009**, *113*, 3168–3175.